



Ag₃PO₄/AgSbO₃ composite as novel photocatalyst with significantly enhanced activity through a Z-scheme degradation mechanism

Chen Chen¹ · Lei Wang¹ · Ting Cheng^{2,3} · Xiaoqin Zhang¹ · Zhiyi Zhou¹ · Xiao Zhang^{2,3} · Qi Xu¹

Received: 30 March 2021 / Accepted: 16 July 2021 / Published online: 24 July 2021
© Iranian Chemical Society 2021

Abstract

In this work, a new composite photocatalyst, combined with Ag₃PO₄ and AgSbO₃ (AZA Catalyst), was elaborately designed, successfully synthesized, and characterized by many techniques, such as XRD, UV-DRS, SEM-EDS, XPS, and TEM. Then, the AZA Catalyst was applied for the photocatalytic degradation of Methylene Blue (MB) and tetracycline. The results showed that AZA Catalyst could effectively degrade MB and tetracycline, and the degradation efficiencies were better than that of sole Ag₃PO₄ and AgSbO₃. The photocatalytic properties of AZA Catalyst also exhibited excellent stabilities. In addition, the active species of ·OH and ·O₂⁻ were demonstrated in the photochemical reaction and played a crucial role to the photocatalytic reaction. Moreover, with the help of advanced characterization (XRD, XPS, ESR, PL, electrochemical analysis) and DFT calculation, the photocatalytic degradation mechanism illustrated that Ag produced in the process of reaction constructed a typical Z scheme path (Ag₃PO₄/Ag/AgSbO₃). Furthermore, due to the work function differences among Ag₃PO₄, AgSbO₃, and Ag, the photogenerated electrons and holes could be effectively transferred and decreased the recombination probability of electrons and holes and thus accelerated the photocatalytic efficiencies of pollutants.

Keywords Photocatalyst · Ag₃PO₄ · AgSbO₃ · Z-scheme mechanism · DFT calculation

Introduction

In recent years, issues of organic wastewater continue to attract wide attention due to its large discharge, complex composition, great harm, and difficult treatment. The main treatment techniques include biological degradation [1], physical and chemical process [2], adsorption [3, 4], membrane separation [5], advanced oxidation [6], and photocatalytic techniques [7]. Among these methods, photocatalysis is new type of treatment technology for organic wastewater arousing considerable attention in these decades. According to studies [8, 9], photocatalytic technology provides us an

ideal thinking for the utilization of energy and the restoration of environment. As reported in early publications, it can transfer the solar energy with low density into the chemical energy with high density and apply to the production of H₂ [10], the reduction of CO₂ [11, 12], photocatalytic disinfection [13], efficient organic transformation [14], and the fixation of N₂ [15]. It can also achieve the degradation of organic pollutants [16] and the reduction of heavy metals [17] in wastewater. Therefore, the photocatalysis is one of the most promising strategies that realize the improvement of energy and the purification of environment.

The main mechanism of photocatalytic technique oxidizing and reducing pollutants in wastewater is to use the electrons and holes generated by semiconductor materials under visible light. In the photocatalytic reaction, the photoexcited electrons can react with the electron acceptors, and photogenerated holes can oxidize the organic molecules [18, 19]. Therefore, the photocatalysts based on semiconductor materials play a crucial role in the degradation of pollutants. To date, many researchers have been devoted efforts to accelerate the photocatalytic activities [20, 21], and the photocatalytic technology has been greatly developed. It was discovered that various types of semiconductor materials

✉ Chen Chen
chenc@just.edu.cn

¹ School of Environmental and Chemical Engineering, Jiangsu University of Science and Technology, Zhenjiang 212100, China

² School of Environmental Ecology, Jiangsu City Vocational College, Nanjing 210017, China

³ Nanjing University and Yancheng Academy of Environmental Technology and Engineering, Yancheng 224000, China

can be used as photocatalysts to accelerate the photocatalytic reactions. These semiconductor materials include TiO_2 [21–23], ZnO [11], BiVO_4 [7], ZrO_2 [24], CdS [25], C_3N_4 [26, 27], Ag_3PO_4 [28], SnO_2 [29], AgSbO_3 [30], and so forth. Among them, Ag_3PO_4 is one of the classic photocatalysts successfully enhancing the photodegradation of pollutants [28, 31]. In addition, the high efficient photocatalytic activity of AgSbO_3 under visible light radiation has also been confirmed by many researchers. Singh proved that AgSbO_3 could play as an efficient photocatalyst that enhanced the photodegradation of organic compounds under visible light [30]. Chen pointed out that AgSbO_3 could be synthesized from crystalline NaSbO_3 and AgSbO_3 , and it displayed excellent photocatalytic performance in the degradation of pollutants [32]. Theoretically speaking, each photocatalytic material has its own specific energy band structure, and thus, the redox abilities of photoexcited electrons and holes produced by single material are very limited. Accordingly, to promote the photocatalytic activities and optimize the photodegradation performance, great efforts have been made by scientists to focus on the composite photocatalytic materials. They could also offer trapping sites for the photoexcited electrons, accelerate the separation of charge, and improve the efficiency of quantum [33, 34]. At present, the composite techniques of photocatalyst materials mainly include elements doping, p – n heterojunctions, and Z-scheme photocatalysts. Among these methods, Z-scheme composite strategy, the energy figure for the transfer of photogenerated carrier formed like a letter “Z,” is one of the most potential photocatalyst composite methods. It was explained that Z-scheme photocatalysts could effectively improve the probability of electron–hole separation and enhance the ability of electron hole redox [35–37]. Besides, it was proposed that they could solve the problems of wide band gap and the recombination of electron and hole pair.

In this work, the composite catalyst (AZA Catalyst) was synthesized by the combination of Ag_3PO_4 and AgSbO_3 . The properties of AZA Catalyst were fully characterized by modern analytical instruments. The characterizations were mainly contained the X-ray diffraction (XRD), the scanning electron microscopy–energy-dispersive spectroscopy (SEM–EDX), the UV–Vis diffuse reflection spectra (DRS), the X-ray photoelectron spectroscopy (XPS), the transmission electron microscope (TEM), and so on. Then, the photocatalytic efficiencies of AZA Catalyst were investigated by photodegradation experiments of Methylene Blue (MB) and tetracycline in solution. To clarify the photocatalytic reaction processes, the impact factors including reaction time, reaction kinetics, the trapping agents, and the recycle performance and stability of photocatalyst were studied. Moreover, we attempted to illustrate the photocatalytic mechanism with the aid of the solid photoluminescence (PL), the electron spin resonance (ESR), electrochemical test, Vienna Ab initio

Simulation Package (VASP) software, and spin-polarized density functional theory (DFT) theory calculation. Through the analysis of photocatalytic mechanism, the efficient photocatalyst, AZA Catalyst, was considered to be coming from the Z-scheme degradation path as $\text{Ag}_3\text{PO}_4/\text{Ag}/\text{AgSbO}_3$.

Experiment and methods

Synthesis of photocatalyst

In experiments, we prepared Ag_3PO_4 , AgSbO_3 , and $\text{Ag}_3\text{PO}_4/\text{AgSbO}_3$ composite materials. The preparation steps of Ag_3PO_4 were as follows: 2 g of PVP (polyvinylpyrrolidone) powder was dispersed in 200 ml of distilled water, and 2.4 g of AgNO_3 was added to the solution with magnetic stirring. Then, 0.84 g of Na_2HPO_4 powder was dispersed in distilled water and then mixed with PVP- AgNO_3 solution with magnetic stirring for 1 h. After that, the mixture was centrifuged through a low-speed benchtop centrifuge. Then, the precipitation substance was washed by ethanol for several times and dried at 80 °C in an air blast drying oven to constant weight.

The preparation procedures of AgSbO_3 were as follows: 0.005 mol of $\text{NaSbO}_3 \cdot 3\text{H}_2\text{O}$ was dispersed in 80 ml of distilled water, and 0.003 mol of AgNO_3 was mixed in the solution with magnetic stirring at 50 °C for 2 h. Then, the mixture was conducted hydrothermal reaction in a stainless steel reactor. During the reaction process, the reaction temperature was 120 °C, and the reaction time was 12 h. After that, the reacted substance was cooled, filtered, and washed with distilled water. Then, the reaction product was dried at 75 °C in the air blast drying oven. Afterward, the product was grounded into finer particles using an agate mortar.

The preparation procedures of $\text{Ag}_3\text{PO}_4/\text{AgSbO}_3$ composite material were as follows: 0.005 mol of $\text{NaSbO}_3 \cdot 3\text{H}_2\text{O}$ was added into 80 ml of distilled water, and AgNO_3 was gradually dispersed in the solution under vigorous agitation. Then, Ag_3PO_4 precipitation (gaining from above steps) was added into the mixture. The mixture was stirred at 50 °C for 2 h. Afterward, this mixture was transferred to a stainless steel reactor to perform hydrothermal reaction and maintained at 120 °C for 12 h. After cooling down to room temperature naturally, the reaction product was obtained by filtered, washed with water, and finally dried at 75 °C in the oven.

Materials characterization

To prove the properties of synthesized materials, we characterized materials using various modern instruments. The X-ray diffraction was recorded by a Shimadzu XD-3A diffractometer, employing $\text{Cu-K}\alpha$ radiation ($\lambda = 1.54056 \text{ \AA}$). The morphologies of materials were observed through HITACHI (S-3400N) scanning electron

microscopy–energy-dispersive spectroscopy. The X-ray photoelectron spectroscopy was conducted using a PHI 5000 VersaProbe XPS equipment. Transmission electron microscope analysis was measured using a FEI Super-X EDS Detector (FEI Talos F200s). The UV–Vis diffuse reflection spectra were obtained using a PerkinElmer Ultraviolet Spectrophotometer (Shimadzu Corporation, UV-3600). The liquid specific surface area of photocatalyst was analyzed through Xigo Liquid Specific Surface Area Determinator. Moreover, the particle size distribution was measured by Malvern Mastersizer 2000 Laser Particle size Analyzer. The solid photoluminescence was measured using a HITACHI Fluorescence Spectrometer (F-7000) equipped with a Xe lamp at room temperature. The active species were detected by the electron spin resonance and using electron paramagnetic resonance spectrometer (EMX micro-6/1/P/L, Karlsruhe, Germany). The DMPO (5, 5-dimethyl-1-pyrroline *N*-oxide) was used as free radical ($\cdot\text{O}_2^-$ and $\cdot\text{OH}$) trapping agent to obtain the signals. The electrochemical impedance spectroscopy and electrochemical photocurrent (interval 20 s) were detected by a CHI 660E electrochemical workstation.

Photocatalytic degradation experiments

The photocatalytic experiments were performed via degrading MB and tetracycline under visible light irradiation (300 W of Xe lamp). In each experiment, the photocatalyst was added into 30 ml of MB or tetracycline solution. (The initial concentration was 20 mg/l.) The mixture was placed into a transparent photoreaction vessel to react, and all experiments were performed at 25 °C. Besides, the reaction time ranged from 10 to 30 min, and the light was turned on at 0 min. After the reaction was completed, the concentration of MB and tetracycline was detected by ultraviolet visible spectrophotometer at a wavelength of 662 nm and 360 nm, respectively. To illustrate the possible photocatalytic mechanism in this reaction, we analyzed the reactive species generated in the process of photocatalytic reaction. Different trapping agents were added into the reaction mixture. These scavenging chemicals, using to quench the reactive species ($\cdot\text{OH}$ and $\cdot\text{O}_2^-$), were EDTA-2Na (0.037 g), TBA (*tert*-butyl alcohol, 0.0094 g), BQ (1,4-benzoquinone, 0.0108 g), and CCl_4 (0.0142 g), respectively. The generation of reactive species by photocatalyst was further proved by ESR instrument.

Meanwhile, the photocatalytic degradation performance of recycled samples was performed in this experiment. The photodegradation efficiencies of MB and tetracycline were detected through a consecutive three cycles. After each reaction of recycled cycle, the photocatalyst was filtered out, and the filter substances were washed by water until

it is neutral. Then, the samples were dried at 75 °C in the air blasting drying oven to a constant weight for the next cycle.

DFT calculation

We used spin-polarized density functional theory and Vienna Ab initio Simulation Package software to perform the DFT calculation [38]. Besides, Perdew–Burke–Ernzerhof functional (PBE) was used to calculate the exchange–correlation potential within the generalized gradient approximation (GGA) method. In addition, the cutoff energy was 450 eV during the calculation, and the *K*-points grids for dimensions were $5 \times 5 \times 5$. The surface model of Ag_3PO_4 , AgSbO_3 , and Ag is displayed in Fig. 1. The work function was also computed through the surface models. The vacuum slab of surface model for Ag_3PO_4 , AgSbO_3 , and Ag was all designed as 30 Å. In the process of theoretical calculation, in order to obtain the optimal structure model, the three material structures were firstly optimized, including atomic coordinates and cell parameters. As seen from Fig. 1, the theoretical surface structures of Ag_3PO_4 , AgSbO_3 , and Ag are all cell units. It included 6Ag, 2P, and 8O atoms for Ag_3PO_4 , 6Ag, 6Sb, and 18O atoms for AgSbO_3 , 2Ag atoms for Ag, respectively.

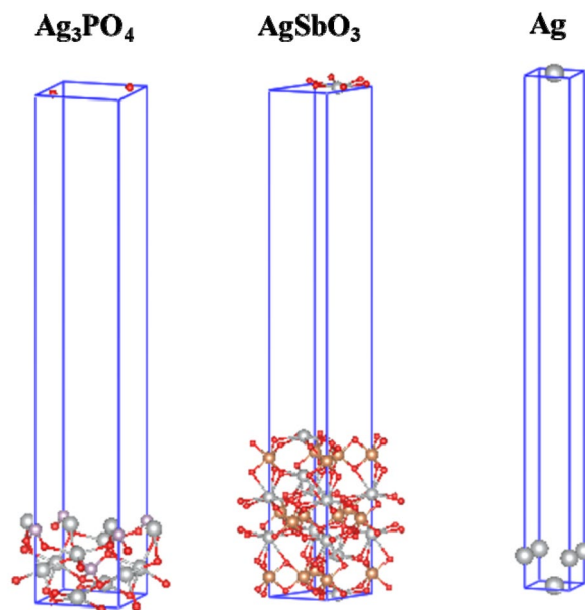


Fig. 1 The theory surface model (Ag_3PO_4 , AgSbO_3 , and Ag) for work function calculation (purple ball is P atom, coffee ball is Sb atom, red ball is O atom, and gray ball is Ag atom)

Results and discussion

Particle size distribution and liquid specific surface area

Figure 2a depicts the analysis result of the particle size distribution of AZA catalyst. It was observed that the particle size distribution of the material exhibited a bimodal structure, which implied that the material contained two substances. Combined with other analysis methods, we believed that the particles in the range of 0.02–0.7 μm were mainly AgSbO_3 , and the particles distributed in the range of 0.7–10 μm were mainly KBiO_3 particles. Figure 2b depicts the analytical results of the liquid-phase surface area for AZA Catalyst. According to the fitting calculation of instrument software, the liquid specific surface area of ANS Catalyst was about 471 m^2/g .

XRD

The phase of composition and crystal structure of Ag_3PO_4 , AgSbO_3 , and AZA Catalyst were obtained by XRD analysis, as shown in Fig. 3. For the XRD pattern of Ag_3PO_4 , the characteristic diffraction peaks could be observed at 2θ , 20.9°, 29.7°, 33.3°, 36.6°, 47.8°, 52.7°, 55.2°, 57.3°, 61.6°, and 71.9° corresponding to the standard peaks of Ag_3PO_4 (PDF#06-0505). For AgSbO_3 , peaks appeared at 2θ , 22.4°, 29.4°, 30.2°, 33.7°, 35.1°, 50.4°, and 60.3°, which were in line with other AgSbO_3 results in the literature [32]. In addition, both the chief XRD peaks of Ag_3PO_4 and AgSbO_3 appeared in the XRD pattern of AZA Catalyst, which indicated that AZA Catalyst was a composite material of Ag_3PO_4 and AgSbO_3 .

UV–Vis diffuse reflection spectra

UV–Vis diffuse reflection spectra were utilized to investigate the optical properties of Ag_3PO_4 , AgSbO_3 , and AZA

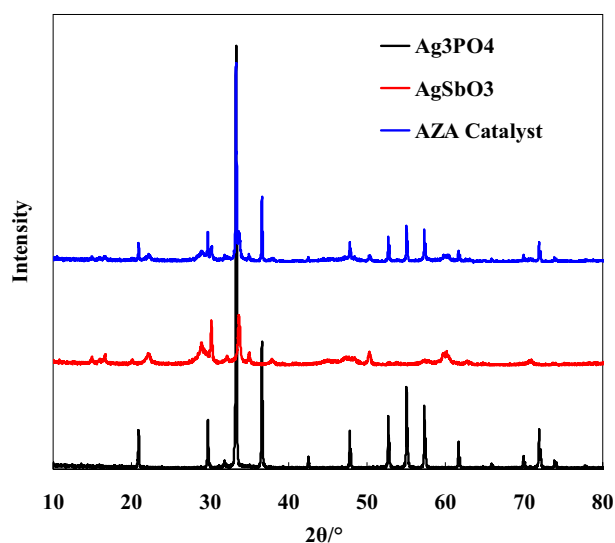


Fig. 3 XRD patterns of Ag_3PO_4 , AgSbO_3 , and AZA Catalyst

Catalyst, as shown in Fig. 4. It was observed that the broad absorption bands of Ag_3PO_4 , AgSbO_3 , and AZA Catalyst were all ranged from 460 to 520 nm. This indicated that the capacities of visible light absorption of Ag_3PO_4 , AgSbO_3 , and AZA Catalyst were all excellent.

Generally speaking, the band gap energy is computed through the Tauc equation [29, 39].

$$\alpha(\nu)h\nu = A(h\nu - E_g)^{n/2} \quad (1)$$

where α , h , ν , A , and E_g are absorption coefficient at light frequency ν , Planck constant, light frequency, a constant, and band gap energy, respectively. For direct transition semiconductor as Ag_3PO_4 and AgSbO_3 , the value of n is 1.

To obtain the value of E_g , the curve of $[a(\nu)h\nu]^2$ versus $h\nu$ could be fitted on the basis of Tauc equation and extrapolated the linear part to zero absorption coefficient. The analysis results are depicted in Fig. 4b. The band gap energy of Ag_3PO_4 and AgSbO_3 exhibited in Fig. 4b was

Fig. 2 Particle size distribution and liquid specific surface area results of AZA Catalyst

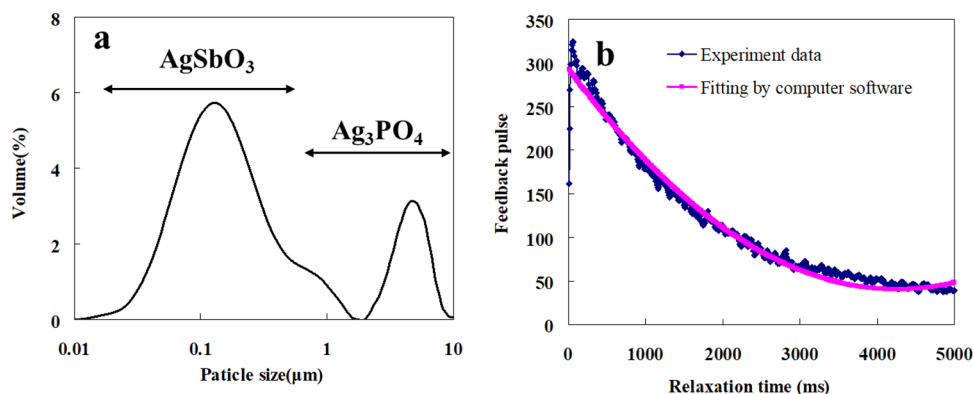
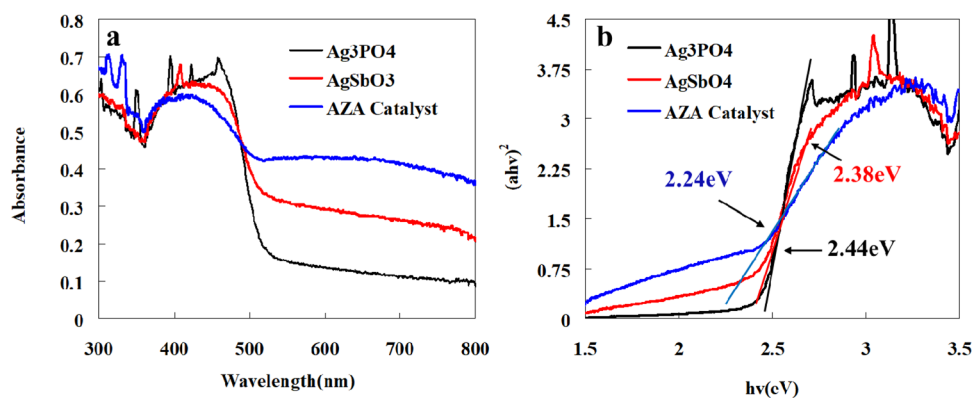


Fig. 4 UV–Vis diffuse reflection spectra of Ag_3PO_4 , AgSbO_3 , and AZA Catalyst



2.44 eV and 2.38 eV, respectively, and they were similar to the other results [30, 40], while for AZA Catalyst, the band gap energy was 2.24 eV, which was a little smaller than that of Ag_3PO_4 and AgSbO_3 . These findings suggested that the combination of Ag_3PO_4 and AgSbO_3 could reduce the band gap. Meanwhile, this combination made AZA Catalyst obtain excellent absorption efficiency for visible light.

SEM–EDX

Figure 5 shows the SEM and EDX analysis results of AgSbO_3 . It could be seen that the material exhibited amorphous morphology in nanoscale. In addition, the particle size of material ranged from 100 to 500 nm. These findings were in line with other studies [30]. The EDX element

mappings of Ag and Sb are depicted in Fig. 5c and d. It could be observed that the elements of Ag and Sb were spread in the location where particles emerged in Fig. 5b. We compared Fig. 5c with Fig. 5d, and it showed that the spread of Ag element was similar to that of Sb element, which further confirmed that the material synthesized was AgSbO_3 .

Figure 6 exhibits the SEM and EDX analysis result of AZA Catalyst. We observed from Fig. 6a that the surface of larger particle (ranged from 2 to 3 μm) was attached to the extremely smaller particles (ranged from 100 to 200 nm). Combined with the analysis results of Fig. 5, it was inferred that the smaller particles might be AgSbO_3 , and the larger particles might be Ag_3PO_4 . EDX analysis suggested that the chemical composition of AZA Catalyst

Fig. 5 The SEM results of AgSbO_3 (a and b) and the EDX element mapping of Ag (c), Sb (d)

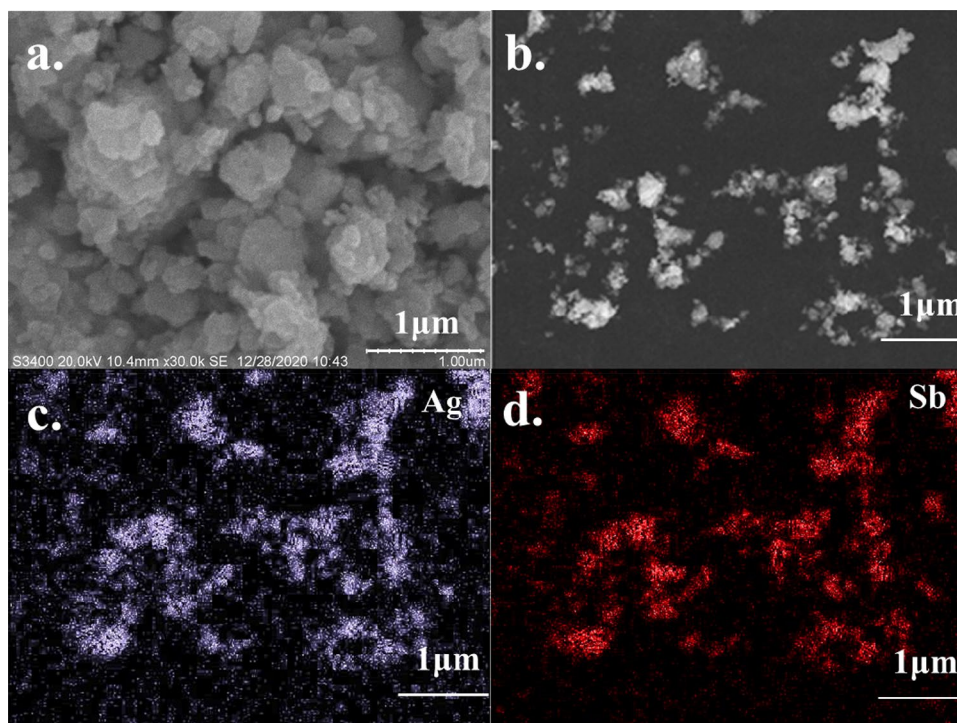
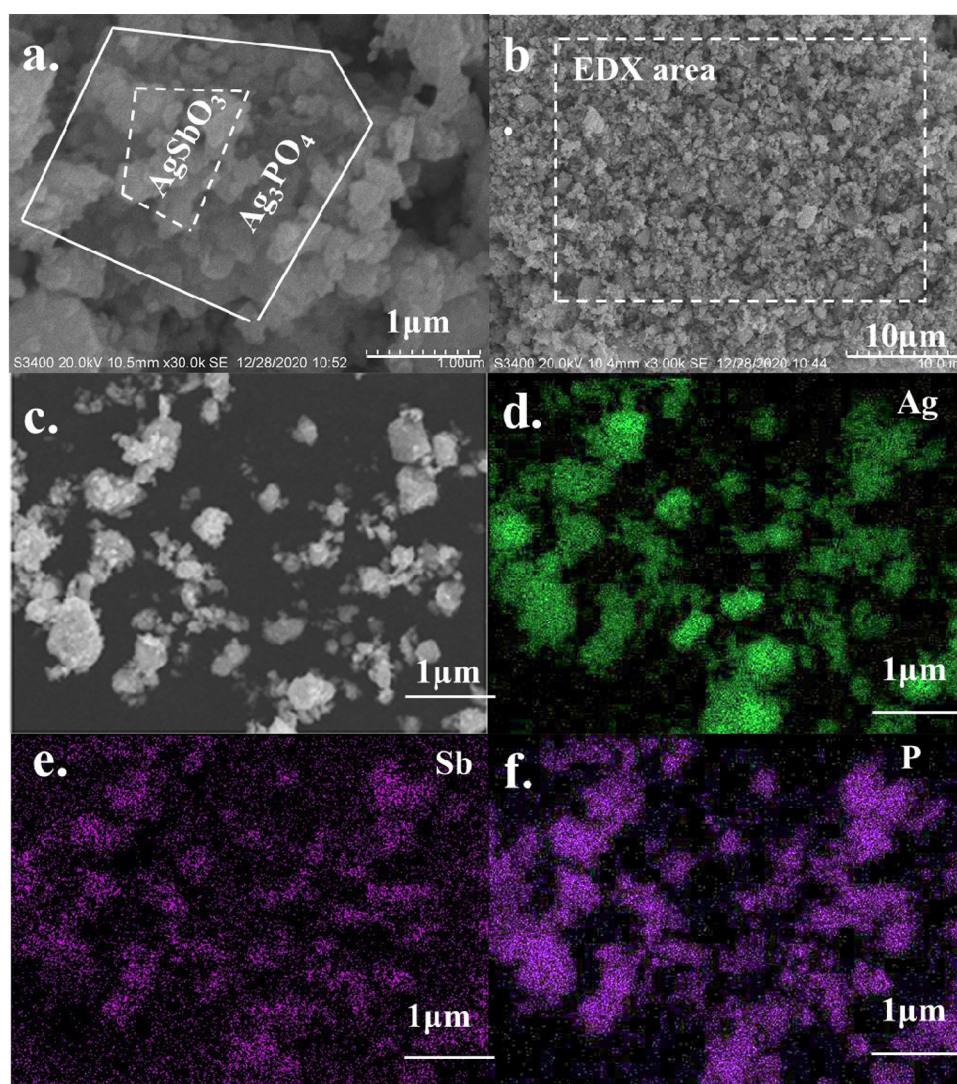


Fig. 6 The SEM results of AZA Catalyst (**a** and **c**), EDX analysis area of AZA Catalyst (**b**) and the EDX element mapping of Ag (**d**), Sb (**e**), and P (**f**)

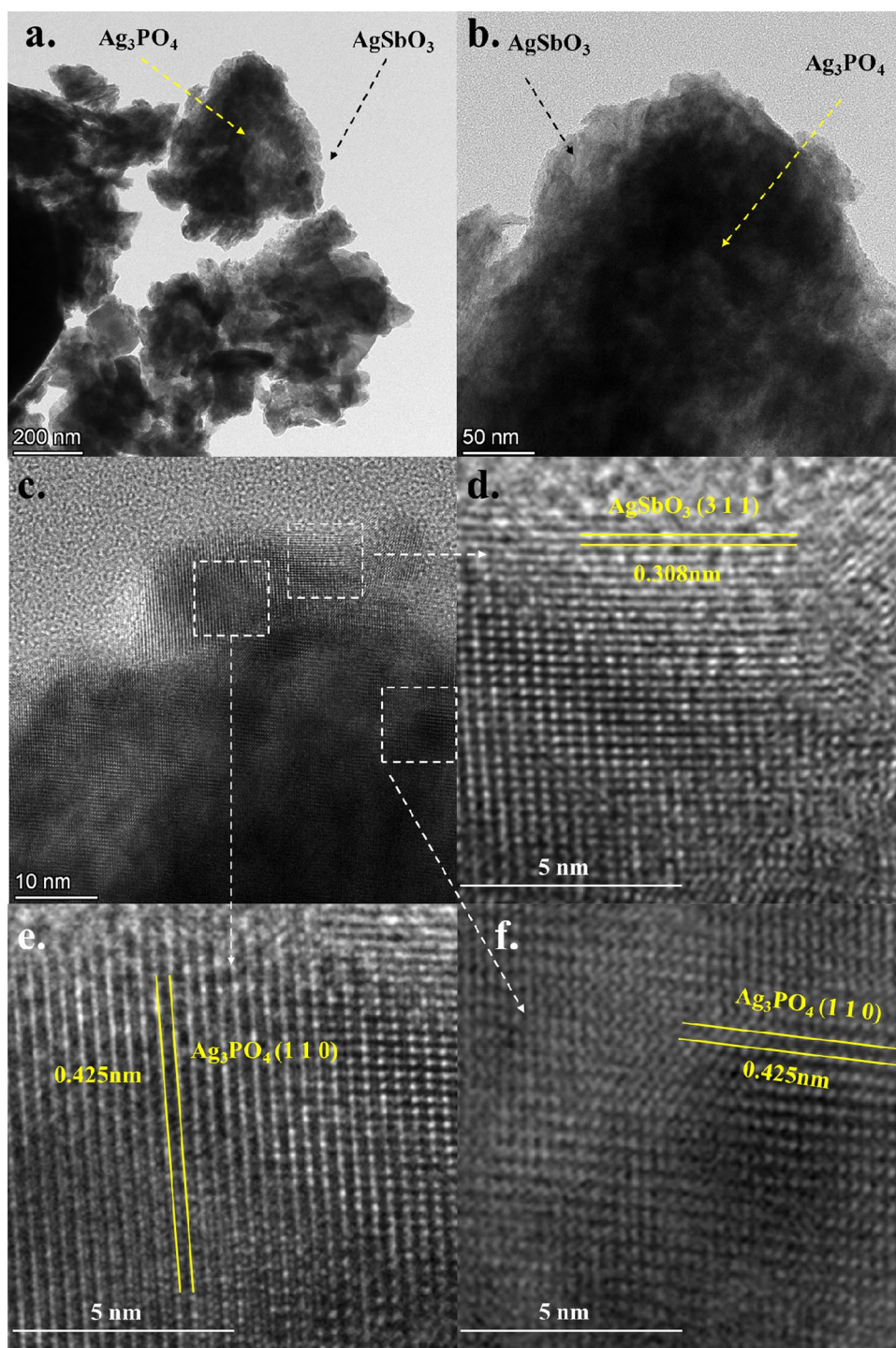


(Fig. 6b area, atomic percent/%) was 66.52% O, 3.32% P, 18.07% Ag, and 12.09% Sb. This element proportion was basically consistent with EDX results. The EDX element mappings of Ag, Sb, and P are described in Fig. 6d–f. It was observed that all the elements of Ag, Sb, and P were mainly spread in the areas where particles emerged in Fig. 6b. These analytical findings were further indicated that AZA Catalyst was a composite material from Ag_3PO_4 and AgSbO_3 . We compared Fig. 6d and f with Fig. 6e, and it was observed that the spread of Sb was looser than that of Ag and P. This phenomenon could be ascribed to the element of P deriving from the smaller particles which was coated on the surface of Ag_3PO_4 . In summary, the analytical results of SEM and EDX confirmed that the AZA Catalyst composite (Ag_3PO_4 and AgSbO_3) was successfully synthesized.

TEM

In the process of experiments, we further verified that AZA Catalyst composite (Ag_3PO_4 and AgSbO_3) was successfully combined via the TEM and HRTEM image, as shown in Fig. 7. It is observed from Fig. 7a and b that the surface of large particles was surrounded by smaller nanoamorphous substances, which was consistent with the result of the SEM. Due to the dispersion before TEM test, the particle size observed by TEM was smaller than that displayed in SEM analysis. The inner dark bigger particles should be Ag_3PO_4 , and the outer transparent amorphous substances should be AgSbO_3 . In addition, as shown in the HRTEM image (Fig. 7c–f), the crystalline interplanar spacing preliminary determined was 0.308 nm and 0.425 nm corresponding to the AgSbO_3 (3 1 1) and Ag_3PO_4 (1 1 0) crystal plane [41],

Fig. 7 The TEM image of AZA Catalyst (**a** and **b**) and HRTEM image of AZA Catalyst (**c–f**)



respectively. This result further confirmed that inner particles were Ag_3PO_4 and the outer transparent amorphous substances were AgSbO_3 .

XPS

We used XPS instrument to further analyze the surface chemical composition of AZA Catalyst, as shown in

Fig. 8. It was described that the dominating peaks of AZA composite catalyst were C1s (282.5 eV), O1s (529.5 eV), Ag3d (366.7 eV and 372.8 eV), Ag3p (570.2 eV), Sb3d (538.9 eV), Sb3p (767.5 eV and 811.8 eV). Except for the element of carbon (for the testing needs), all the other elements could be observed in AZA Catalyst, and this findings were consistent with other analytical results of characterization techniques. XPS results suggested that the

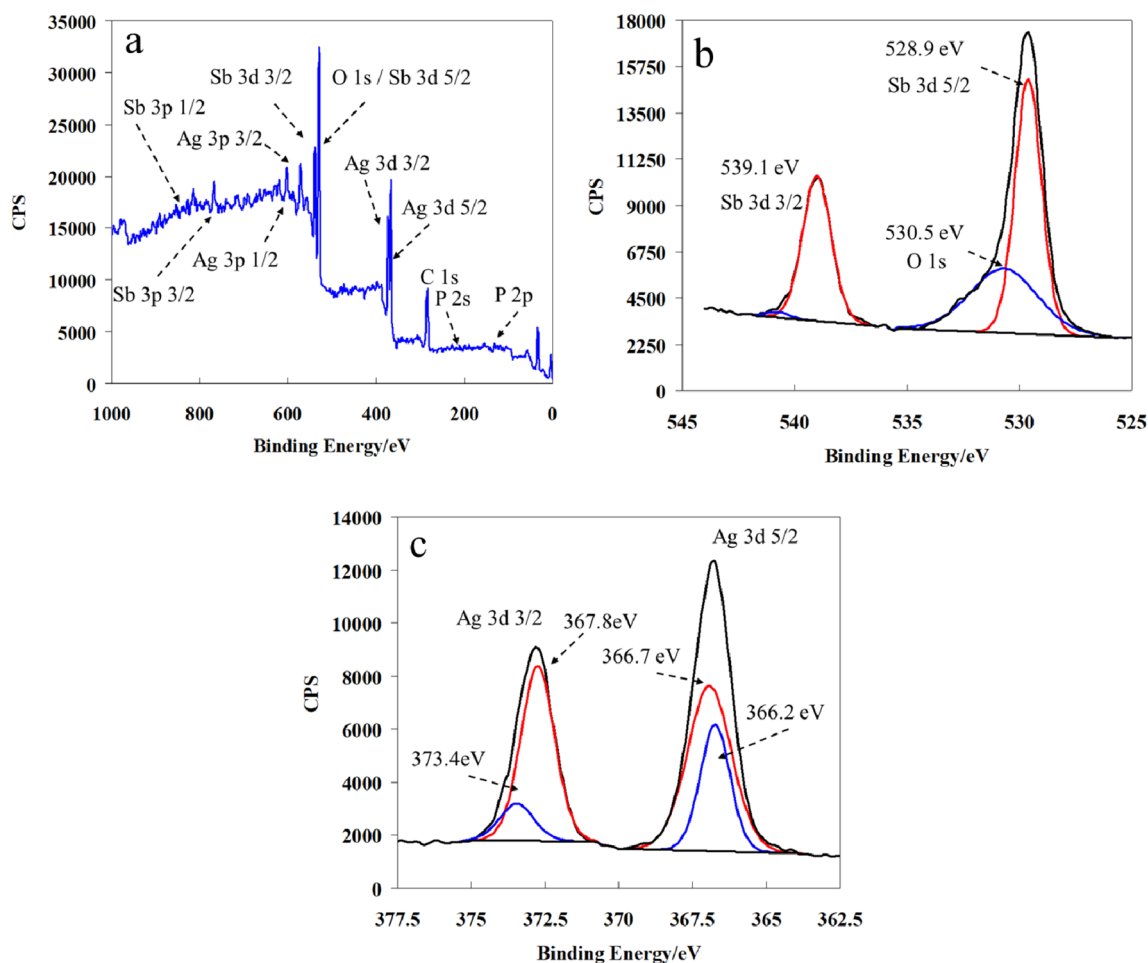


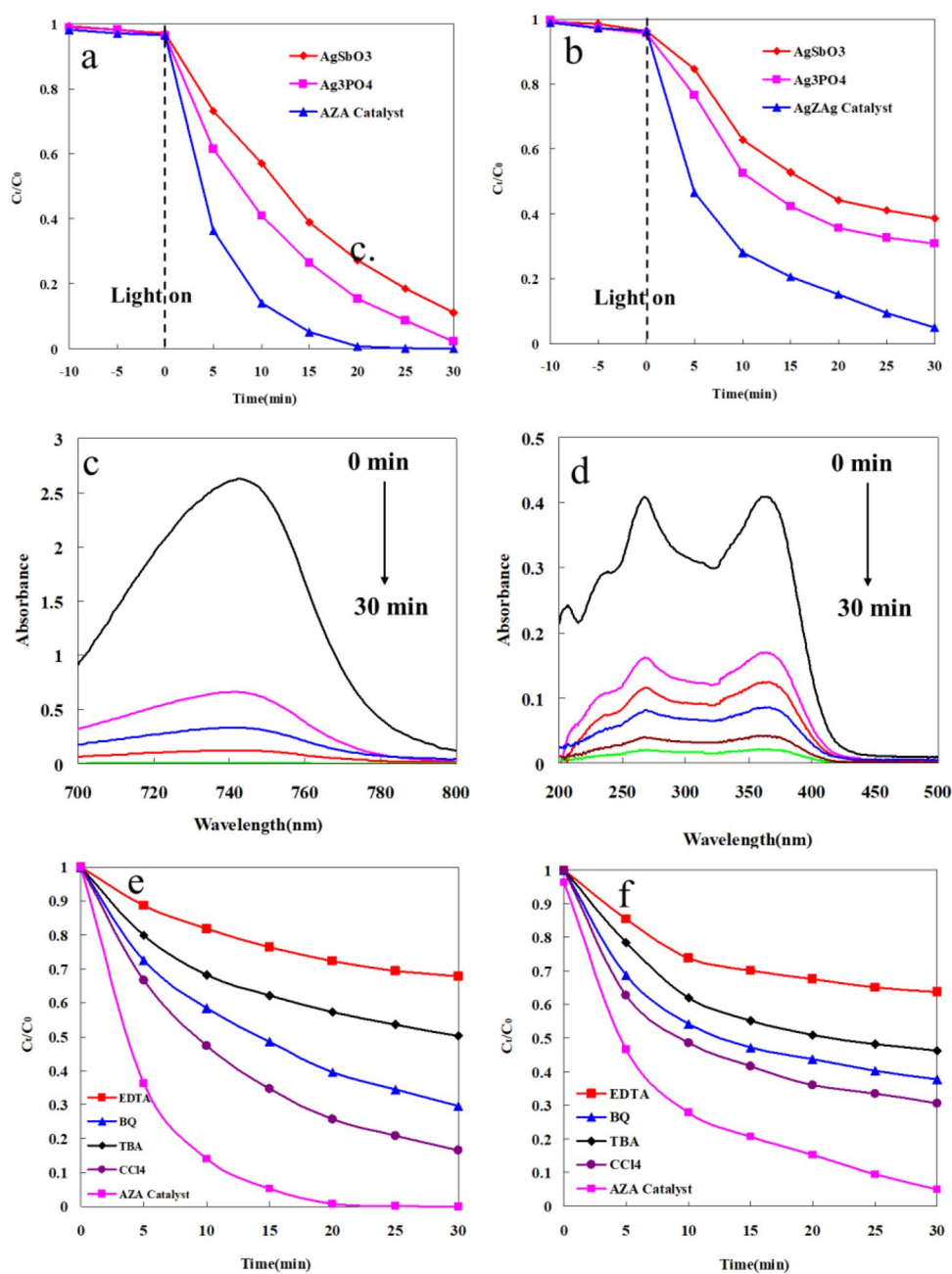
Fig. 8 The wide scanning XPS spectra of AZA Catalyst (a); the high-resolution XPS spectrum of O1s (b), Sb 3d (b), and Ag3d (c)

chemical composition of AZA Catalyst (atomic percent/%) is 67.2% O, 2.4% P, 18.9% Ag, and 11.5% Sb. This element proportion was basically consistent with EDX results. In addition, more details could be obtained from the high-resolution XPS spectra of O1s and Sb3d (Fig. 8b). Moreover, it was observed that the peak of 529.5 eV could be divided into two individual peaks (528.9 eV and 530.5 eV). On account of the binding energies of O1s close to that of Sb3d_{5/2}, we inferred that the peak at 530.5 eV was attributed to O1s, and the peak at 528.9 eV was ascribed to Sb3d_{5/2}. Besides, the shift of binding energy for O (from 531.8 to 530.5 eV) might be due to the bonds between O and other elements. Additionally, it is observed from Fig. 8c that the peaks of Ag3d_{5/2} could be divided into two parts at 366.6 eV and 366.9 eV. Similarly, the peaks of Ag3d_{3/2} could also be decomposed into 372.7 eV and 373.4 eV. This phenomenon might be attributed to different Ag atoms from Ag₃PO₄ and AgSbO₃ molecules.

Photocatalytic activity

Figure 9 depicts the photocatalytic degradation results of MB and tetracycline. In Fig. 9a and b, we compared the photodegradation efficiencies of Ag₃PO₄, AgSbO₃, and AZA Catalyst under visible light, and the Xe lamp was turned on at 0 min. Meanwhile, changes of the removal rates for pollutants were obtained at the stage between – 10 and 0 min, and this accelerated the uniform mixing of pollutants with catalysts at this stage. It was observed that there was almost no change of degradation for pollutants in the absence of visible light (from – 10 to 0 min). And then, the pollutants were gradually degraded under the visible light. In addition, the degradation effect of MB and tetracycline with AZA Catalyst was best among the three catalysts, which indicated that the photocatalytic degradation efficiency was optimal in AZA Catalyst system than that of Ag₃PO₄ and AgSbO₃ system. For instance, the residual rate was approaching 0 at

Fig. 9 The photodegradation process of MB (a) and tetracycline (b); UV–visible absorption spectrum of MB (c) and tetracycline (d) degraded by AZA Catalyst; the photodegradation efficiency of MB (e) and tetracycline (f) by addition of trapping agents

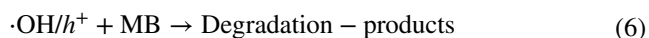
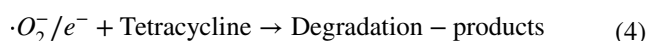
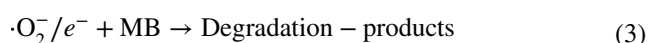
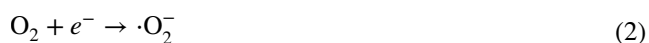


20 min with AZA Catalyst, whereas they were 15.4% and 27.3% with Ag₃PO₄ and AgSbO₃ as catalysts, respectively. Similarly, the trend was also observed for the photodegradation of tetracycline (Fig. 9b), and the AZA Catalyst still displayed optimal photocatalytic activity than Ag₃PO₄ and AgSbO₃. Take the reaction time of 15 min; for example, the residual rate of tetracycline with Ag₃PO₄, AgSbO₃, and AZA Catalyst system was 42.3%, 52.75, and 20.7%, respectively. These findings verified that the combined utilization of Ag₃PO₄ and AgSbO₃ (AZA Catalyst) significantly enhanced the photodegradation efficiencies of pollutants. Moreover, changes of UV–visible absorption spectra of MB

and tetracycline with reaction time are depicted in Fig. 9c and d. It was observed that the curves of MB and tetracycline gradually declined with the reaction time, which confirmed that both MB and tetracycline could be photodegraded under AZA Catalyst system.

According to references [7, 42], photocatalysts play a crucial role in the photodegradation process of organic pollutants, and they can release the strong redox such as free electrons, holes, and related free radicals to accelerate the reaction procedure. In addition, it is essential for us to identify which species are active during the photocatalytic degradation reaction. Accordingly, the trapping agents are

utilized to quench the reactive species through adding to the reaction solution. It is believed that EDTA-2Na is used as a hole trapper, BQ can be played as an oxygen free radical trapper, TBA is utilized as a scavenger for hydroxyl radical, and CCl_4 is considered as an electron trapper. Figure 9e and f depicts the photodegradation efficiencies of MB and tetracycline after adding different scavengers. It was observed that the photodegradation efficiencies of MB and tetracycline were all decreased after adding these trapping agents, which proved that these scavenging chemicals could effectively inhibit the photocatalytic activities in this reaction. Therefore, it was probably that the photodegradation path from Eqs. (2)–(7) was took place in the reaction process. Moreover, it was obvious that TBA and EDTA-2Na as scavengers displayed more impacts on the photodegradation effect of pollutants. Accordingly, we inferred that the active species, hydroxyl radicals and holes, were probably captured by the scavengers, which seriously impacted the photocatalytic activities and then decreased the removal efficiencies of pollutants. Furthermore, the main degradation path of MB and tetracycline from Eqs. (5)–(7) with AZA Catalyst under visible light was likely to illustrate this phenomenon.



In this study, the first-order reaction model was utilized to evaluate the apparent degradation kinetics during the reaction process. The equation of first-order reaction model was as follows. The constant k in the reaction could be acquired through modeling the related experimental results and Eq. (8) [43–45].

$$\ln\left(\frac{C}{C_0}\right) = -kt \quad (8)$$

where C_0 is the initial concentration of pollutant; C_t is the concentration of pollutant at time t .

On the basis of the experimental data in Fig. 9a and b, the fitting results of apparent kinetics are displayed in Fig. 10a and b. The R^2 values in three photocatalytic systems of Ag_3PO_4 , AgSbO_3 , and AZA Catalyst were all above 0.95. Accordingly, the first-order reaction kinetics could be used

to satisfactorily model the apparent photodegradation process of MB and tetracycline. Besides, the k value of AZA Catalyst system (Fig. 10c, d) was the highest compared with other systems.

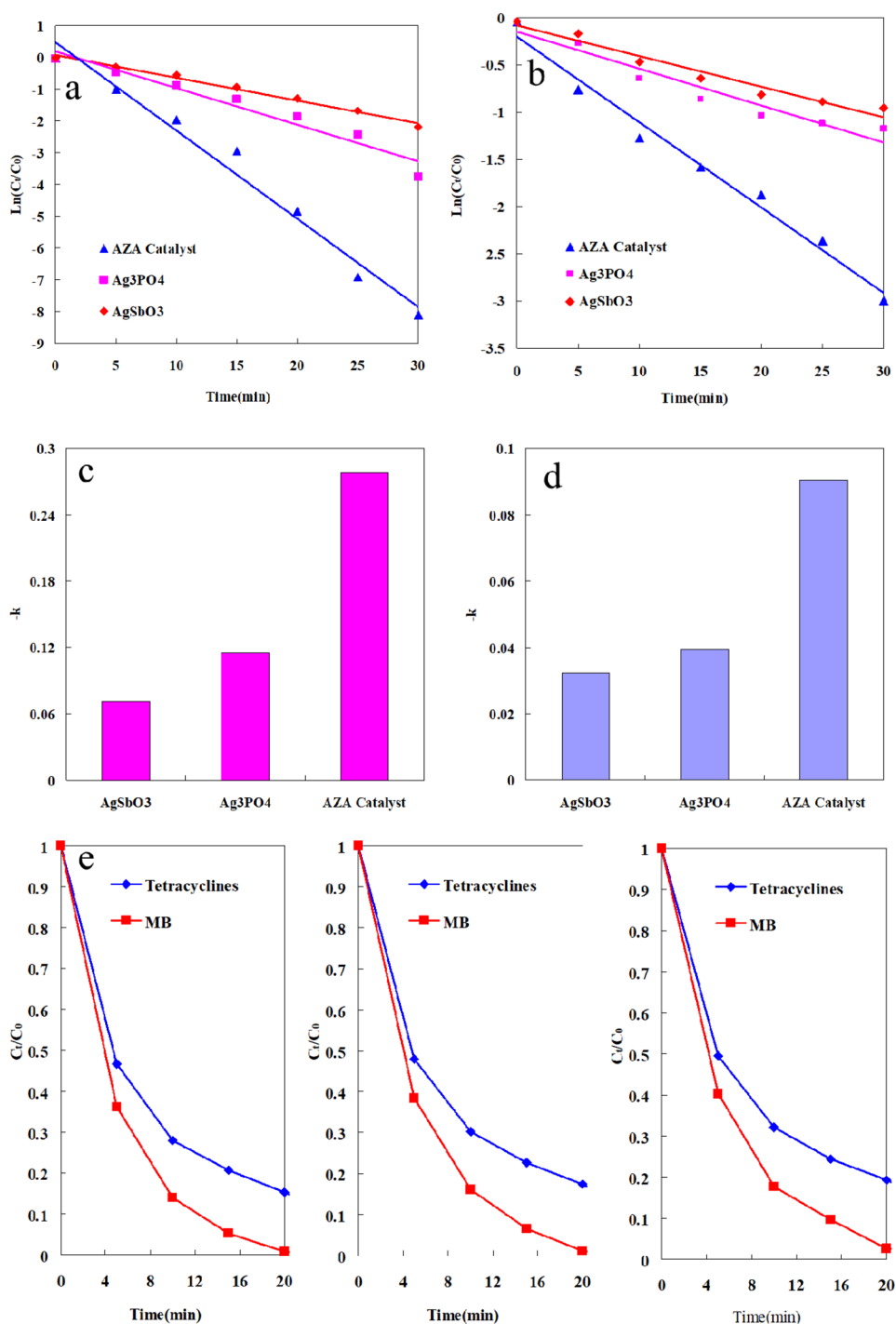
The reusing performance of photocatalyst was crucial to the application. Therefore, to evaluate the stability of AZA Catalyst, the photodegradation efficiencies of pollutants after reusing for three times with under the same conditions were investigated, as shown in Fig. 10e. It was observed that there was basically no obvious attenuation of photodegradation effect after three times of cycles for MB and tetracycline. This finding proved that AZA Catalyst exhibited excellent photocatalyst stability. During the process of photodegradation, the photocatalytic activity of AZA Catalyst was slightly decreased after the cycle reactions, which might be due to the mass loss of material in the cycles.

Photocatalytic degradation mechanism

To illustrate the photodegradation mechanism of pollutants with AZA Catalyst, the samples of catalyst after photocatalytic reaction (named AZA Catalyst-light) were collected and characterized. Figure 11a depicts the comparison curves of XRD patterns between AZA Catalyst and AZA Catalyst-light. It was observed that the XRD patterns for two samples were very similar, which indicated that the composition and structure of AZA Catalyst were maintained stable during the photocatalytic reaction. We also observed a new faint peak (at 2θ : 38.1°) from XRD patterns of AZA Catalyst-light. According to standard spectra and related references [46, 47], the new diffraction peak might be ascribed to the (1 1 1) surface of silver (PDF#65-2871). The new formed silver was probably come from the decomposition of Ag_3PO_4 under visible light [47]. In addition, the XPS analysis was used to examine the surface chemical compositions of AZA Catalyst-light, as shown in Fig. 11b and c. The primary curves of AZA Catalyst-light were also contained C1s, O1s, Ag3d, Ag3p, Sb3d, and Sb3p. This analytical result further proved the AZA Catalyst obtained excellent stability in the photocatalytic reaction. XPS results suggested that the chemical composition of AZA Catalyst (atomic percent/%) is 74.5% O, 1.5% P, 16.5% Ag, and 7.5% Sb. The decrease in P content implies the decomposition of Ag_3PO_4 . Besides, through observing the high-resolution XPS spectra of Ag3d, it was discovered that the peaks of $\text{Ag}3d_{5/2}$ could be divided into three parts at 365.8 eV, 366.5 eV, and 366.9 eV. Similarly, the peaks of $\text{Ag}3d_{3/2}$ could be decomposed into 372.5 eV, 372.8 eV, and 373.2 eV. Additionally, the new low XPS peaks at 365.8 eV and 373.2 eV might be ascribed to the silver formed during the photocatalytic reaction [41, 46].

The transient photocurrent responses of AgSbO_3 , Ag_3PO_4 , AZA Catalyst, and AZA Catalyst-light under Xe lamp irradiation are depicted in Fig. 12a. It was seen

Fig. 10 The apparent fitting results (**a** MB and **b** tetracycline) using the pseudo-first-order reactions; the constants of the first-order reactions for the MB (**c**) and tetracycline (**d**); degradation curves of photocatalyst reuse (**e**)



that sole AgSbO₃ showed the lowest response among the four photocatalytic systems, implying that AgSbO₃ was probably unable to form enough electrons and holes under visible light. On the contrary, the photocurrent intensity of sole Ag₃PO₄ was much stronger than AgSbO₃, while it declined gradually with the irradiation time. According to the related studies, the decrease in signals for Ag₃PO₄ might be due to the photocorrosion. In addition, after the

combination usage of Ag₃PO₄ and AgSbO₃, the photocurrent intensity of AZA Catalyst was enhanced significantly, proving that AZA Catalyst possessed stronger reflecting ability for visible light. Moreover, it was obvious that the photocurrent intensity of AZA Catalyst-light was the highest, and it also displayed excellent stability. That implied the production of silver during the photocatalytic reaction was helpful to efficiently generate and transfer

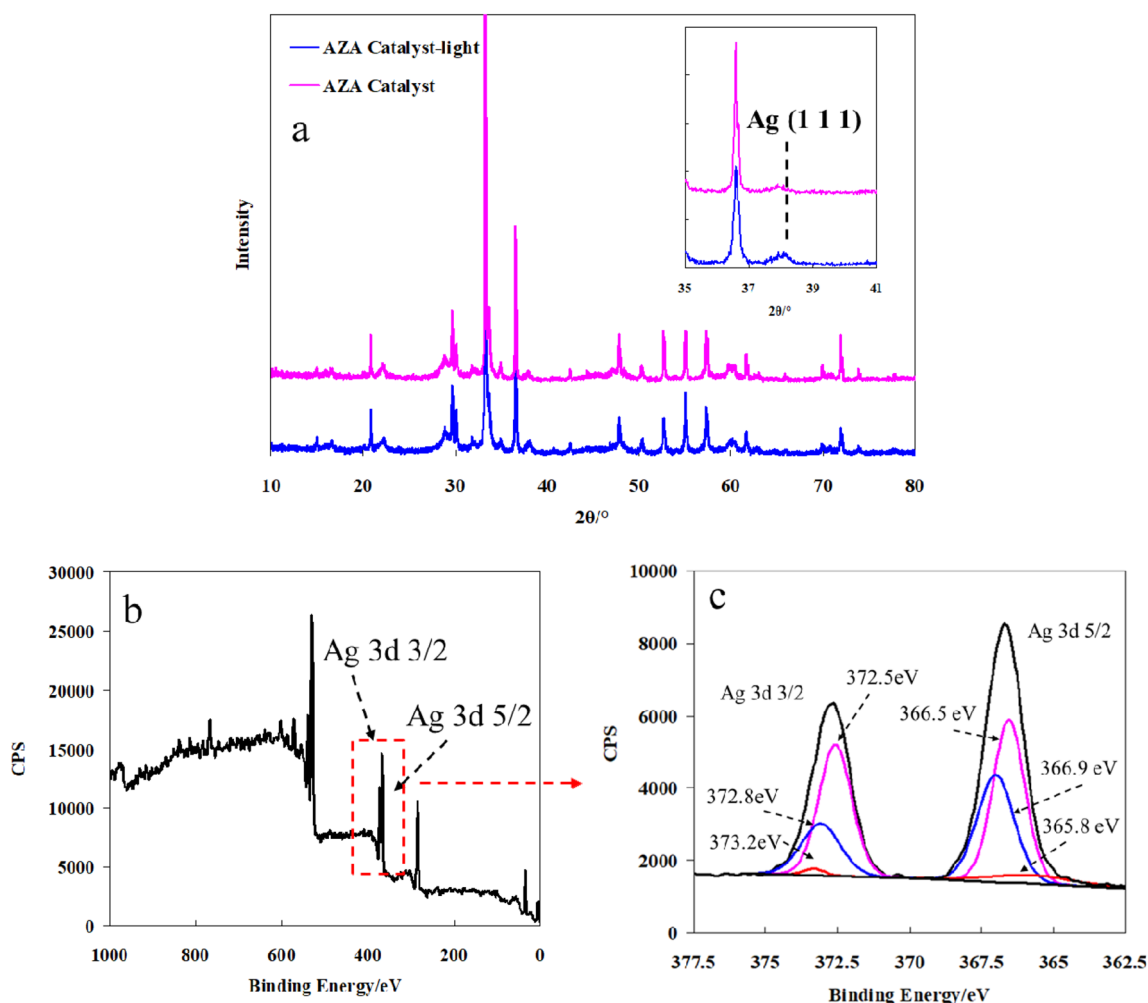


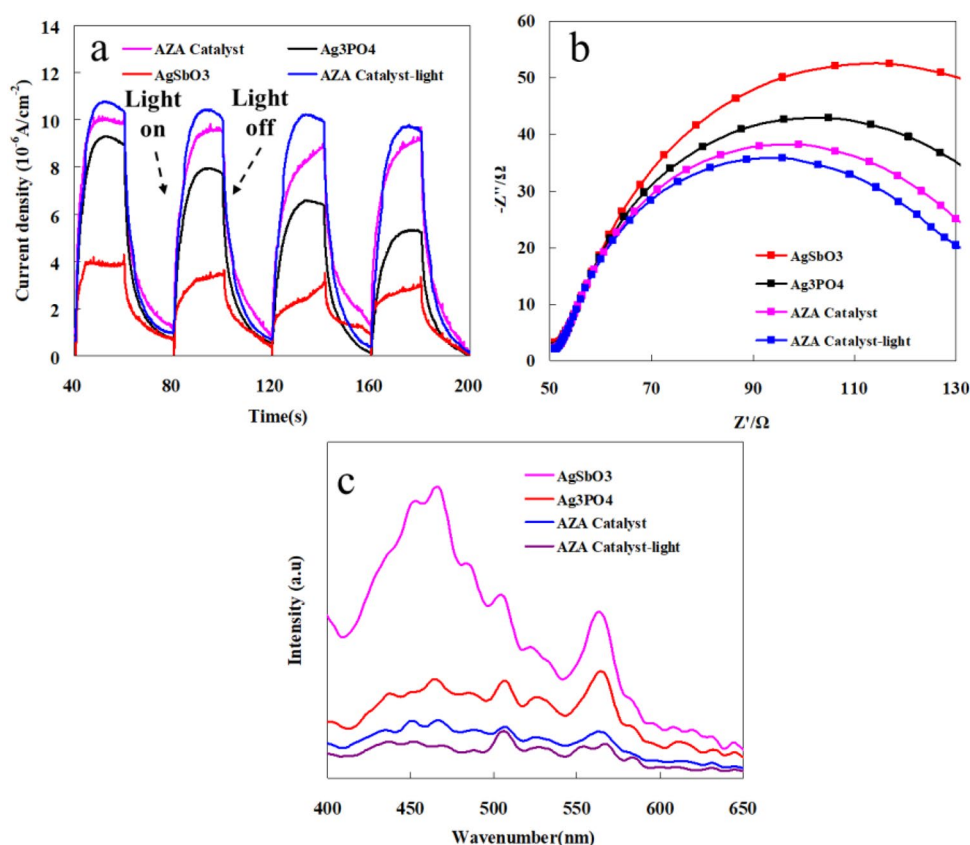
Fig. 11 XRD patterns of AZA Catalyst-light (a); the wide scanning XPS spectra of AZA Catalyst-light (b); the high-resolution XPS spectra of Ag3d (c)

the photoinduced electrons and holes. Furthermore, we utilized EIS to analyze the size of charge transfer resistance and the efficiency of charge separation. Figure 12b depicts the EIS value of AgSbO_3 , Ag_3PO_4 , AZA Catalyst, and AZA Catalyst-light. Obviously, the radius values of AZA Catalyst-light were the smallest compared with other photocatalysts, indicating that the forming Ag probably reduced the resistance of charge transfer and thus effectively promoted the photocatalytic reaction process. Additionally, the PL emission spectra were further conducted to evaluate the combination and separation of photogenerated electrons and holes, as displayed in Fig. 12c. It was observed that the photoluminescence spectra intensity of AgSbO_3 was the highest than others, suggesting that the photoinduced electrons and holes produced by AgSbO_3 obtained great recombination possibility. After the combination of Ag_3PO_4 with AgSbO_3 , the recombination possibility of AZA Catalyst was greatly reduced, and the

curves obtained were lower than that of Ag_3PO_4 . We also observed that the AZA Catalyst-light displayed the lowest photoluminescence spectra intensity. This phenomenon might due to the production of silver further give rise to the decrease in the combination probability.

Figure 13 shows the TEM and HRTEM image of AZA Catalyst-light. In general, the TEM analysis results of AZA Catalyst-light were similar to those of AZA Catalyst. The results showed that some smaller nanoamorphous substances (AgSbO_3) surrounded the surface of larger particles (Ag_3PO_4). In addition, as shown in the HRTEM image (Fig. 13c–f), the crystalline interplanar spacing preliminary determined was 0.267 nm, 0.307 nm, and 0.236 nm, corresponding to the Ag_3PO_4 (2 1 0), AgSbO_3 (3 1 1), and Ag (1 1 1) [41] crystal plane, respectively. The appearance of Ag (1 1 1) crystal plane indicated the formation of Ag particles in AZA Catalyst-light, which was consistent with the result of XPS analysis.

Fig. 12 Transient photocurrent responses (a), electrochemical impedance spectra (b), and steady-state PL spectra (c) of AgSbO₃, Ag₃PO₄, AZA Catalyst and AZA Catalyst-light



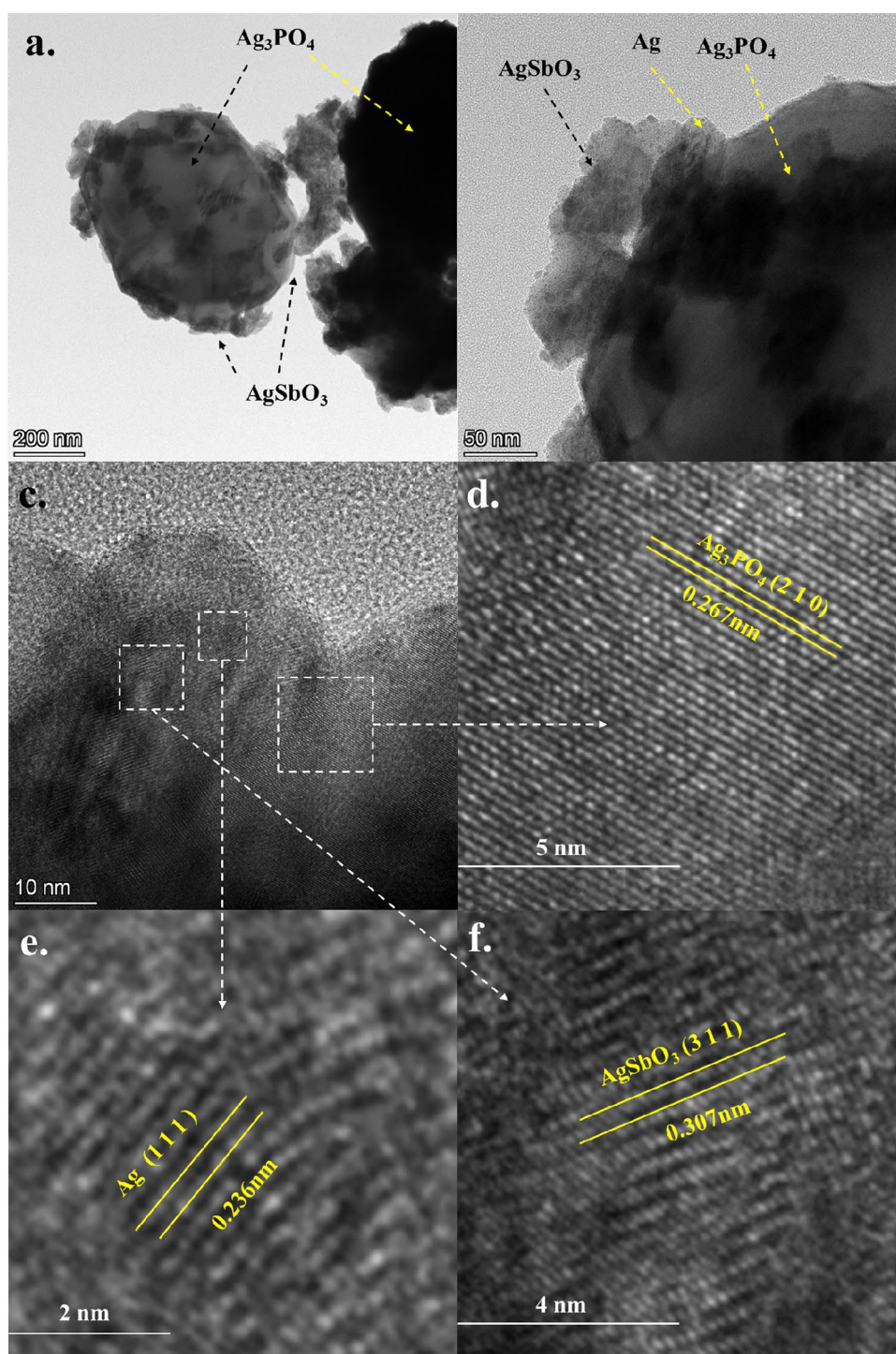
ESR spin-trapping spectra were used to detect the relative content of hydroxyl radicals (DMPO- \cdot OH) and the superoxide radicals (DMPO- \cdot O₂⁻) by DMPO technique, and the analytical results are depicted in Fig. 14. It was observed that no signal peaks of \cdot OH or \cdot O₂⁻ were detected in dark condition. This result indicated there were no excited electrons and holes in the absence of visible light. In contrast, under the condition of light, both AZA Catalyst and AZA Catalyst-light systems had obvious signal peaks of \cdot OH (with the intensity ratio of 1:2:2:1) and \cdot O₂⁻, demonstrating that both \cdot OH and \cdot O₂⁻ were participating in the photocatalytic reaction. These findings were also consistent with Fig. 9e and f. For the degradation of pollutants, the reactive radicals might play an essential role in the photocatalytic reaction. We also found from Fig. 14 that the typical peak intensity of \cdot OH and \cdot O₂⁻ in AZA Catalyst-light system was stronger than that of AZA Catalyst system, indicating that the AZA Catalyst-light system could produce more \cdot OH and \cdot O₂⁻ in the photocatalytic reaction, which further proved the production of silver was helpful to the photocatalytic reaction, thereby enhancing the photodegradation efficiencies of pollutants.

Figure 15 displays the Mott–Schottky plots for Ag₃PO₄ (a) and AgSbO₃ (b). It was observed that the slopes of Mott–Schottky straight line of both Ag₃PO₄ and AgSbO₃ were positive, implying that the two photocatalysts belonged to *n*-type semiconductor materials. It is well

known that the characteristic of *n*-type semiconductor material is that the Fermi energy level is relatively close to the position in the bottom of conduction band. At the same time, the frequency band potential is also approximate to the bottom of conduction band. According to the analysis results of Fig. 15, the frequency band potentials of Ag₃PO₄ and AgSbO₃ were 1.24 V and 0.022 V, respectively. On the basis of the related theories of semiconductor and the previous analytical results for band gap [48], the top of the valence band to the bottom of the conduction band for Ag₃PO₄ was approximately ranged from -6.5 to -4.1 eV, and that ranged from -8.1 to -5.7 eV for AgSbO₃. Since Ag₃PO₄ and AgSbO₃ were both *n*-type semiconductors, thus the Fermi energy level of AgSbO₃ was lower than that of Ag₃PO₄, and the work function of AgSbO₃ was greater than that of Ag₃PO₄.

The position of the Fermi energy level and the size of work function can directly affect the transfer path of photogenerated electrons and holes in the photocatalytic process. According to the previous analytical results, AZA Catalyst produced metallic Ag under the visible light, and the photoelectric effect of AZA Catalyst-light was better than that of AZA Catalyst. Meanwhile, the intensity of \cdot OH and \cdot O₂⁻ generated by AZA Catalyst-light system was stronger than that of AZA Catalyst system (obtained from ESR). These findings proved that the metal Ag produced by AZA

Fig. 13 The TEM image of AZA Catalyst-light (a and b) and HRTEM image of AZA Catalyst-light (c–f)



Catalyst under visible light could effectively promote the photocatalytic reaction.

In order to further clarify the transfer mechanism of photogenerated electrons and holes in this study, we used DFT theory and VASP software to investigate the work function of Ag_3PO_4 , AgSbO_3 , and Ag , as displayed in Fig. 16. The work functions of Ag_3PO_4 , AgSbO_3 , and Ag calculated were 3.98 eV, 5.1 eV, and 4.76 eV, respectively, According to

the classic model of Schottky, because the work function of Ag_3PO_4 was smaller than that of metallic Ag , the photogenerated electrons in Ag_3PO_4 would be transferred to metallic Ag when they contacted with each other. Besides, the transfer would be continued until the Fermi energy level of Ag_3PO_4 and metallic Ag reached the same position. In this situation, the surface of Ag_3PO_4 was positively charged because of lacking electrons, and the surface of metal Ag

Fig. 14 ESR spectra of radical adducts trapped by DMPO in the dark and under visible light irradiation for DMPO- \cdot OH (**a** AZA Catalyst, **b** AZA Catalyst-light); ESR spectra of radical adducts trapped by DMPO in the dark and under visible light irradiation for DMPO- \cdot O $_2^-$ (**c** AZA Catalyst, **d** AZA Catalyst-light)

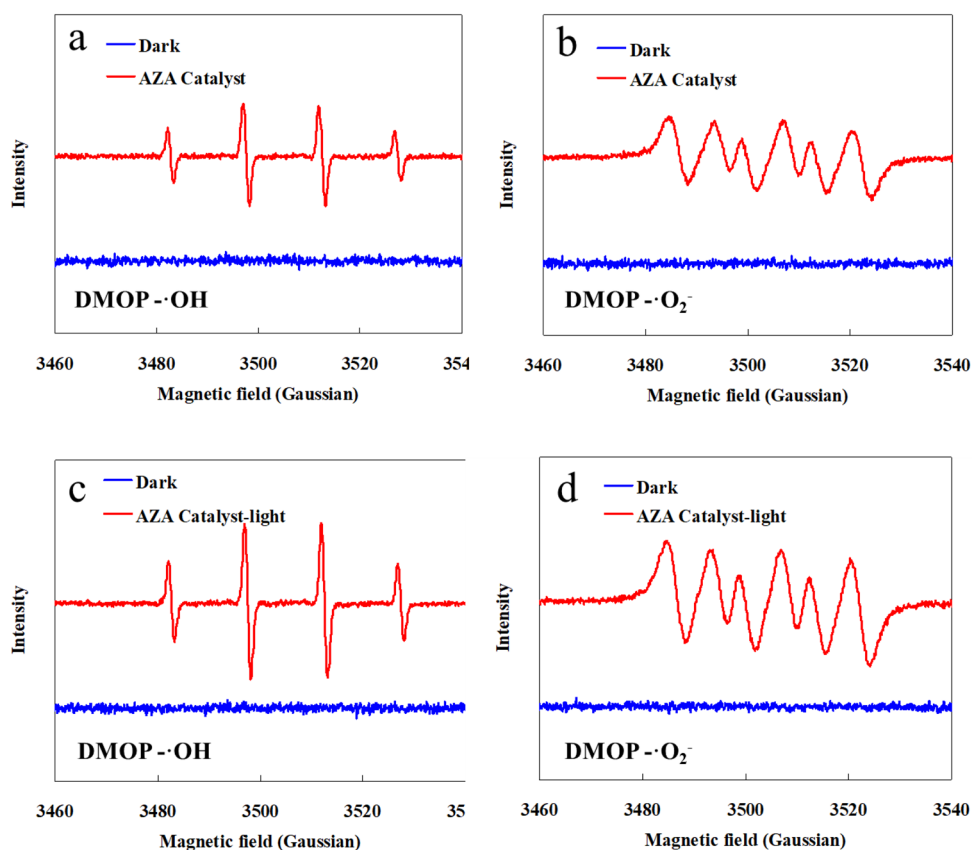
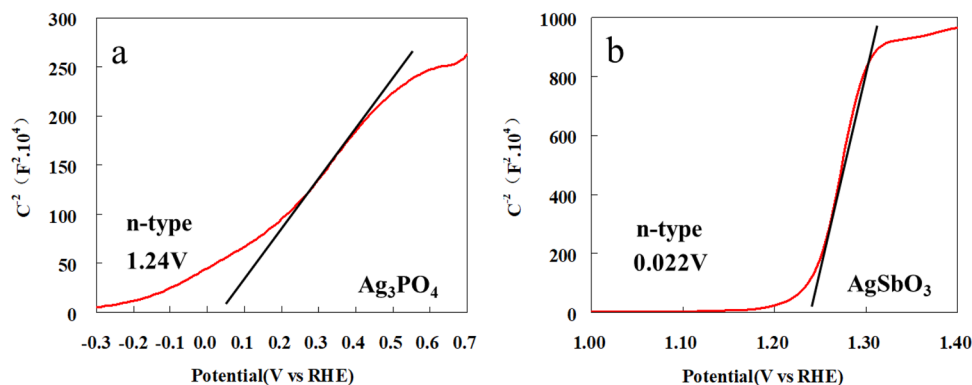


Fig. 15 Mott–Schottky plots for Ag $_3$ PO $_4$ (**a**) and AgSbO $_3$ (**b**)



was negatively charged due to its excess electrons. Therefore, it might generate the potential difference between Ag $_3$ PO $_4$ and Ag, and the direction of electric field was directed from Ag $_3$ PO $_4$ to metal Ag. At this time, a classic Schottky barrier that hindered electron transfer and hole transfer was generated between Ag $_3$ PO $_4$ and metal Ag (Fig. 17). It blocked the transfer of electrons from Ag $_3$ PO $_4$ to metal Ag, while that promoted the transfer of holes from Ag $_3$ PO $_4$ to Ag. Contrary to the situation of Ag $_3$ PO $_4$, when *n*-type AgSbO $_3$ contacted with metal Ag, the Schottky barrier was generated that promoted the transfer of electrons from AgSbO $_3$ to Ag since the work function of AgSbO $_3$ was greater than that of metal

Ag. Simultaneously, it hindered the transfer of holes from AgSbO $_3$ to Ag.

Based on the above analytical theory, we believed that Ag $_3$ PO $_4$, AgSbO $_3$, and metal Ag newly generated formed a typical Z scheme path for the transfer between electron and hole, as shown in Fig. 18. The holes generated by Ag $_3$ PO $_4$ under light excitation and the electrons generated by AgSbO $_3$ would continue to be transferred to metal Ag. In this case, the electrons and holes in Ag $_3$ PO $_4$ and AgSbO $_3$ were effectively separated, which could greatly reduce the

Fig. 16 The work function of Ag_3PO_4 (a), AgSbO_3 (b), and Ag (c) from DFT calculation

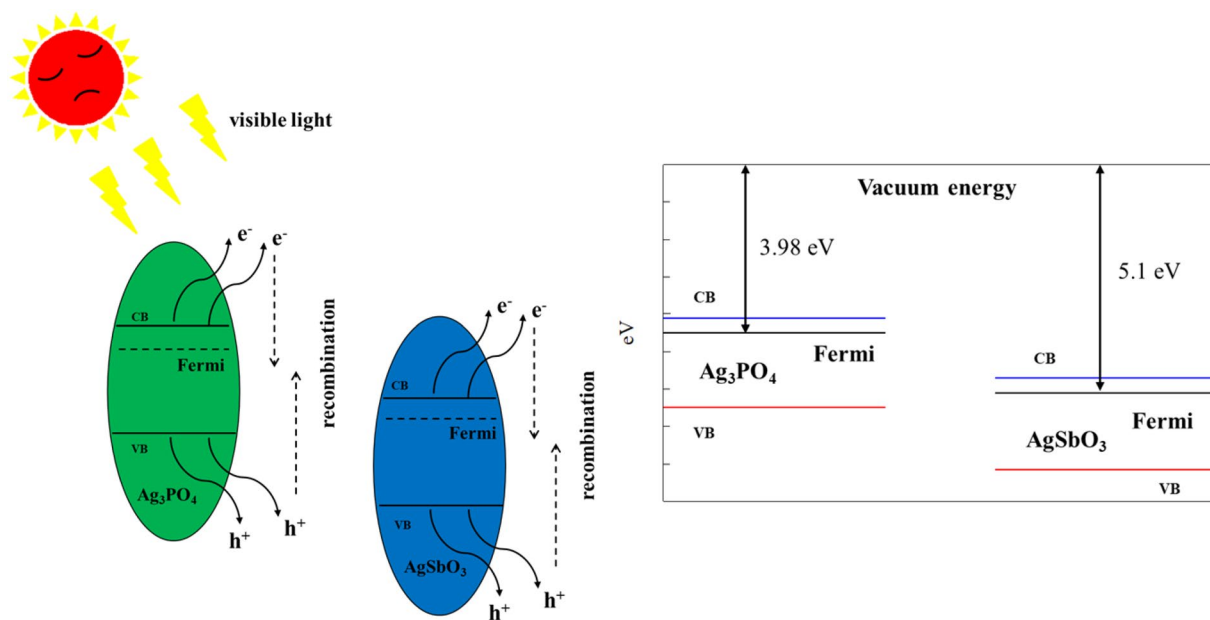
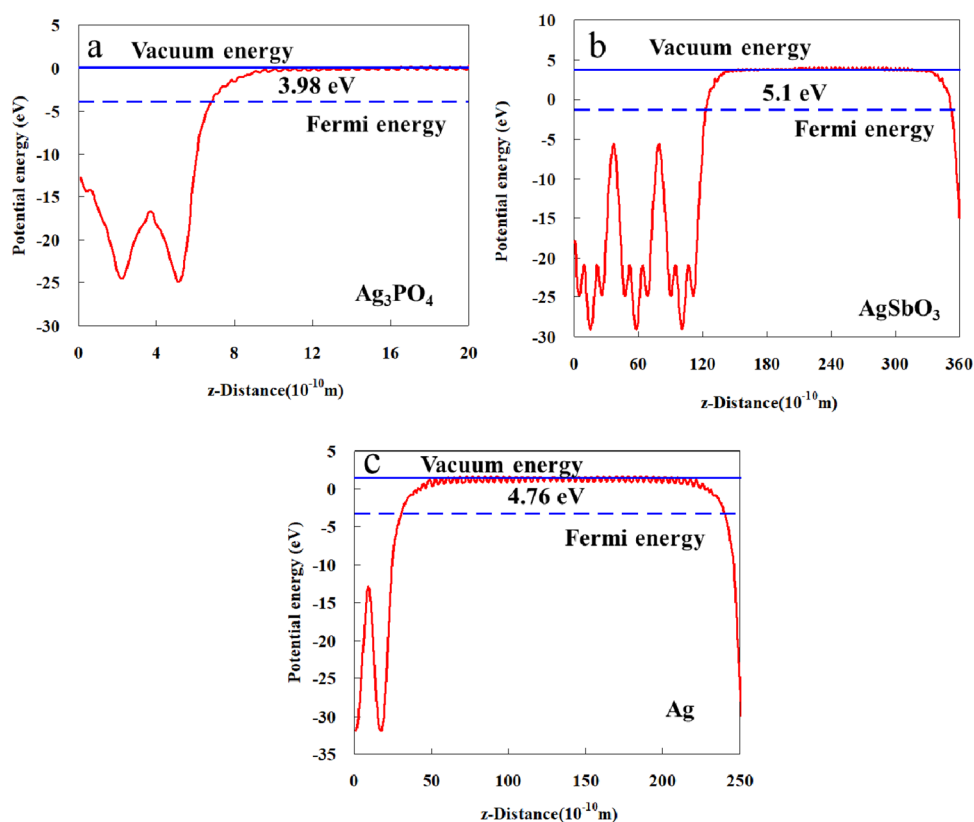


Fig. 17 Photocatalytic mechanism of sole Ag_3PO_4 and AgSbO_3

recombination probability of electrons and holes. Furthermore, the electrons retained in Ag_3PO_4 and the holes in

AgSbO_3 could better degrade pollutants in the solution and improve the photocatalytic effect.

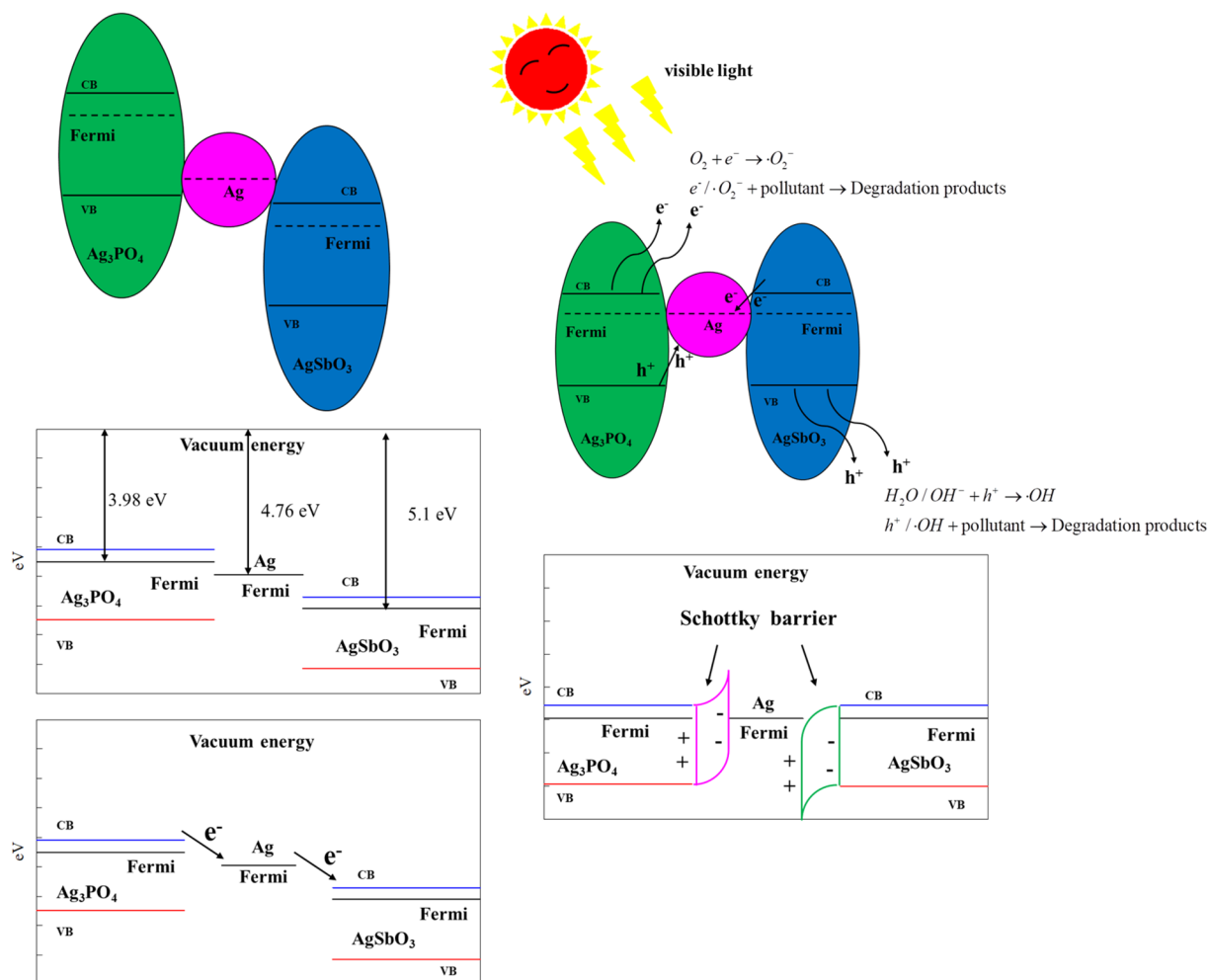


Fig. 18 Photocatalytic mechanism of Z-scheme degradation path ($\text{Ag}_3\text{PO}_4/\text{AZASbO}_3$)

Conclusion

In this work, a composite photocatalyst of AZA Catalyst, combined with Ag_3PO_4 and AgSbO_3 , was synthesized and fully characterized. The photocatalytic activities of AZA Catalyst were evaluated by the photodegradation of MB and tetracycline under visible light. The characterization results demonstrated that the composite AZA Catalyst was successfully synthesized. Besides, the combination of Ag_3PO_4 and AgSbO_3 reduced the band gap, and AZA Catalyst obtained excellent absorption efficiency for visible light. The photocatalytic experiments pointed out that the photocatalytic degradation efficiencies of MB and tetracycline with AZA Catalyst were the best than that of Ag_3PO_4 and AgSbO_3 . In addition, the trapping agents were seriously impacted the photocatalytic activities, and the active species of $\cdot\text{OH}$ and $\cdot\text{O}_2^-$ were vital to the photocatalytic reaction, which was proved by ESR detection. Moreover, the apparent photodegradation process of pollutants was

satisfactorily modeled by the first-order reaction kinetics. The experiments of recycled photocatalytic material confirmed that AZA Catalyst maintained stable and exhibited excellent photocatalytic performance. The electrochemical experiments findings confirmed that AZA Catalyst possessed strong reflecting ability for visible light, and the production of Ag was helpful to efficiently generate and transfer the photoinduced electrons and holes and reduce their recombination possibility. Furthermore, DFT calculation revealed that Ag_3PO_4 , AgSbO_3 , and the newly generated Ag formed a typical Z scheme path for the transfer between electron and hole and realized the separation of electrons and holes and thus effectively promoted the photocatalytic reaction.

Acknowledgements This work is supported by Science Foundation of Jiangsu Colleges and Universities (Grant Nos. 17KJD610001, 17KJD610002) and school-level scientific research platform project of Jiangsu City Vocational College.

References

1. C.H. Wang, Z.L. Peng, K.J. Feng, Z.J. Chen, H.R. Liu, *Environ. Sci. Pollut. Res.* **27**, 22902 (2020)
2. K. Czerwionka, J. Makinia, *Water Sci. Technol.* **70**, 561 (2014)
3. R. Guillossou, J. Le Roux, A. Goffin, R. Mailler, G. Varrault, E. Vulliet, C. Morlay, F. Nauleau, S. Guerin, V. Rocher, J. Gasperi, *Water Res.* **190**, 116749 (2021)
4. X. Zhang, T. Cheng, C. Chen, L. Wang, Q. Deng, G. Chen, C. Ye, *Mater. Res. Express* **7**, 085007 (2020)
5. J.L. Han, X. Xia, M.R. Haider, W.L. Jiang, Y. Tao, M.J. Liu, H.C. Wang, Y.C. Ding, Y.N. Hou, H.Y. Cheng, A.J. Wang, *Sci. Total Environ.* **628–629**, 261 (2018)
6. C. Chen, T. Cheng, *J. Chem. Soc. Pak.* **35**, 243 (2013)
7. T. Cheng, C. Chen, L. Wang, X. Zhang, C. Ye, Q. Deng, G. Chen, *Pol. J. Environ. Stud.* **30**, 2027 (2021)
8. T.P. Hu, K. Dai, J.F. Zhang, S.F. Chen, *Appl. Catal. B Environ.* **269**, 118844 (2020)
9. X.B. Liu, H.Q. Zhuang, *Int. J. Energy Res.* **45**, 1480 (2021)
10. R. Xiao, C.X. Zhao, Z.Y. Zou, Z.P. Chen, L. Tian, H.T. Xu, H. Tang, Q.Q. Liu, Z.X. Lin, X.F. Yang, *Appl. Catal. B Environ.* **268**, 118382 (2020)
11. F. Zhang, Y.H. Li, M.Y. Qi, Z.R. Tang, Y.J. Xu, *Appl. Catal. B Environ.* **268**, 118380 (2020)
12. A. Akhundi, A. Habibi-Yangjeh, M. Abitorabi, S. Rahim Pouran, *Catal. Rev.* **61**, 595 (2019)
13. A. Habibi-Yangjeh, S. Asadzadeh-Khaneghah, S. Feizpoor, A. Rouhi, *J. Colloid Interface Sci.* **580**, 503 (2020)
14. A. Akhundi, A. Badii, G.M. Ziarani, A. Habibi-Yangjeh, M.J. Muñoz-Batista, R. Luque, *Mol. Catal.* **488**, 110902 (2020)
15. X.M. Li, X. Sun, L. Zhang, S.M. Sun, W.Z. Wang, *J. Mater. Chem. A* **6**, 3005 (2018)
16. C.Y. Zhou, G.M. Zeng, D.L. Huang, Y. Luo, M. Cheng, Y. Liu, W.P. Xiong, Y. Yang, B. Song, W.J. Wang, B.B. Shao, Z.H. Li, *J. Hazard. Mater.* **386**, 121947 (2020)
17. C. Zhao, Z.H. Wang, X. Li, X.H. Yi, H.Y. Chu, X. Chen, C.C. Wang, *Chem. Eng. J.* **389**, 123431 (2020)
18. H.J. Dong, X.X. Zhang, J.M. Li, P.J. Zhou, S.Y. Yu, N. Song, C.B. Liu, G.B. Che, C.M. Li, *Appl. Catal. B Environ.* **263**, 118270 (2020)
19. M.M. Dou, J. Wang, B.R. Gao, C. Xu, F. Yang, *Chem. Eng. J.* **383**, 123134 (2020)
20. K.K. Kefeni, B.B. Mamba, *Sustain. Mater. Technol.* **23**, e00140 (2020)
21. D.J. Chen, Y.L. Cheng, N. Zhou, P. Chen, Y.P. Wang, K. Li, S.H. Huo, P.F. Cheng, P. Peng, R.C. Zhang, L. Wang, H. Liu, Y.H. Liu, R. Ruan, *J. Clean. Prod.* **268**, 121725 (2020)
22. A. Habibi-Yangjeh, S. Feizpoor, *J. Iran. Chem. Soc.* **17**, 351 (2019)
23. T.L. Palma, B. Vieira, J. Nunes, J.P. Lourenço, O.C. Monteiro, M.C. Costa, *J. Iran. Chem. Soc.* **17**, 2013 (2020)
24. S.N. Basahel, T.T. Ali, M. Mokhtar, K. Narasimharao, *Nanoscale Res. Lett.* **10**, 73 (2015)
25. K.Y. Lin, L. Feng, D.K. Li, J.W. Zhang, W. Wang, B.J. Ma, *Appl. Catal. B Environ.* **286**, 119880 (2021)
26. X. Huang, F. Guo, M. Li, H. Ren, Y. Shi, L. Chen, *Sep. Purif. Technol.* **230**, 115854 (2020)
27. S. Asadzadeh-Khaneghah, A. Habibi-Yangjeh, *J. Clean. Prod.* **276**, 124319 (2020)
28. S.Y. Li, M. Zhang, Z.H. Qu, X. Cui, Z.Y. Liu, C.C. Piao, S.G. Li, J. Wang, Y.T. Song, *Chem. Eng. J.* **382**, 122394 (2020)
29. D. Selleswari, P. Meena, D. Mangalaraj, *J. Iran. Chem. Soc.* **16**, 1291 (2019)
30. J. Singh, S. Uma, *J. Phys. Chem. C* **113**, 12483 (2009)
31. B.B. Shao, X.J. Liu, Z. Liu, G.M. Zeng, Q.H. Liang, C. Liang, Y. Cheng, W. Zhang, Y. Liu, S.X. Gong, *Chem. Eng. J.* **368**, 730 (2019)
32. D.P. Chen, W. Bowers, S.E. Skrabalak, *Chem. Mater.* **27**, 174 (2015)
33. X.J. Wen, L. Qian, X.X. Lv, J. Sun, J. Guo, Z.H. Fei, C.G. Niu, *J. Hazard. Mater.* **385**, 121508 (2020)
34. P. Raizada, P. Thakur, A. Sudhaik, P. Singh, V.K. Thakur, A. Hosseini-Bandegharai, *Arab. J. Chem.* **13**, 4538 (2020)
35. V. Hasija, P. Raizada, A. Sudhaik, P. Singh, V.K. Thakur, A.A.P. Khan, *Solid State Sci.* **100**, 106095 (2020)
36. D. Majhi, K. Das, A. Mishra, R. Dhiman, B.G. Mishra, *Appl. Catal. B Environ.* **260**, 118222 (2020)
37. M.L. Ren, Y.H. Ao, P.F. Wang, C. Wang, *Chem. Eng. J.* **378**, 122122 (2019)
38. F. Kresse, *Phys. Rev. B Condens. Matter* **54**, 11169 (1996)
39. P. Dumrongrojthanath, A. Phuruangrat, S. Thongtem, T. Thongtem, *J. Iran. Chem. Soc.* **16**, 733 (2019)
40. X.L. Miao, X.Y. Yue, Z.Y. Ji, X.P. Shen, H. Zhou, M.M. Liu, K.Q. Xu, J. Zhu, G.X. Zhu, L.R. Kong, S.A. Shah, *Appl. Catal. B Environ.* **227**, 459 (2018)
41. C. Du, J. Song, S. Tan, L. Yang, G. Yu, H. Chen, L. Zhou, Z. Zhang, Y. Zhang, Y. Su, X. Wen, S. Wang, *Mater. Chem. Phys.* **260**, 124136 (2021)
42. K.T. Wong, S.C. Kim, K. Yun, C.E. Choong, I.W. Nah, B.H. Jeon, Y. Yoon, M. Jang, *Appl. Catal. B Environ.* **273**, 119034 (2020)
43. S. Sohrabnezhad, M.E. Takas, *J. Iran. Chem. Soc.* **16**, 45 (2019)
44. T. Bunluesak, A. Phuruangrat, J. Teppetcharat, P. Patiphatpanya, P. Dumrongrojthanath, S. Thongtem, T. Thongtem, *J. Iran. Chem. Soc.* **18**, 1103 (2020)
45. C. Chen, T. Cheng, X. Zhang, R. Wu, Q. Wang, *J. Chem. Soc. Pak.* **41**, 1034 (2019)
46. F. Chen, Q. Yang, X.M. Li, G.M. Zeng, D.B. Wang, C.G. Niu, J.W. Zhao, H.X. An, T. Xie, Y.C. Deng, *Appl. Catal. B Environ.* **200**, 330 (2017)
47. K. Shen, M.A. Gondal, R.G. Siddique, S. Shi, S.Q. Wang, J.B. Sun, Q.Y. Xu, *Chin. J. Catal.* **35**, 78 (2014)
48. Y. Xu, M.A.A. Schoonen, *Am. Miner.* **85**, 543 (2000)